Research Square

Preprints are preliminary reports that have not undergone peer review.
They should not be considered conclusive, used to inform clinical practice,
or referenced by the media as validated information.

Performance evaluation and microstructural characterization of multi-scale hybrid fiber-reinforced high-content solid waste-based repair materials

Jianjun Zhao
Harbin Institute of Technology
Xunxun Jiang
Harbin Institute of Technology
Yisen Zhao
Inner Mongolia University of Technology
Hao Chen
Harbin Institute of Technology
Junhui Qiao
Institute of Technical Information for Building Materials Industry
Shuang Li
shuangli@hit.edu.cn

Harbin Institute of Technology

Research Article

Keywords: Repair materials, Solid waste, Multi-scale hybrid fibers, Micro-characterization, Theoretical calculation model

Posted Date: November 13th, 2026

DOI: https://doi.org/10.21203/rs.3.rs-11412626/v1

License: This work is licensed under a Creative Commons Attribution 4.0 International License.
Read Full License

Performance evaluation and microstructural characterization of multi-scale hybrid fiber-reinforced high-content solid waste-based repair materials

Jianjun Zhao[1,2,3], Xunxun Jiang[3], Yisen Zhao[4], Hao Chen[3], Junhui Qiao[5], Shuang Li[3]

Abstract: Developing new repair materials with high toughness and high solid waste content is of great significance for improving the service performance of structures and achieving green transformation in engineering. This study used blast furnace slag (BFS) and waste glass powder (WGP) as the main solid waste constituents to prepare multi-scale hybrid fiber-reinforced high-content solid waste-based repair materials (HWRM). Systematic tests were conducted on the HWRM's workability, mechanical properties, and deformation characteristics. The results showed that the fluidity of the repair material can reach up to 269 mm, indicating excellent workability. The influence of solid waste content on strength performance was relatively small, demonstrating good strength retention characteristics. Notably, the tensile strain performance of this material was remarkably improved compared with control group ECC. Its peak tensile strain reached 7.8%, showing superior deformation capacity and crack control performance. In this study, XRD, DTG-TG and SEM techniques were adopted to investigate the hydration mechanism and fiber-bridging effect of HWRM, revealing the intrinsic relationship between macroscopic properties and microscopic structures. A theoretical model for the tensile properties of HWRM was established, achieving prediction accuracy over 90%. The study findings can provide a scientific basis and technical support for the engineering application of HWRM.

Keywords: Repair materials; Solid waste; Multi-scale hybrid fibers; Micro-characterization; Theoretical calculation model

1 Introduction

With the continuous promotion of urbanization and infrastructure construction, concrete buildings, bridges, tunnels and other projects that were built on a large scale in the early years have now entered the middle and later stages of service in large quantities. During long-term service, these concrete structures are subject to multiple factors such as erosion by the natural environment, heavy traffic loads, and material aging [1]. In severe cold regions, the alternating freeze-thaw cycles, characterized by severe cold in winter and mild thaw in summer, are highly prone to damaging the internal pore structure of concrete, leading to surface spalling, efflorescence, and reduced structural compactness. Chloride ions

✉ Shuang Li
shuangli@hit.edu.cn

[1] Key Laboratory of Earthquake Engineering and Engineering Vibration, Institute of Engineering Mechanics, China Earthquake Administration, Harbin 150080, China

[2] Key Laboratory of Earthquake Disaster Mitigation, Ministry of Emergency Management, Harbin 150080, China

[3] Key Lab of Structures Dynamic Behavior and Control of the Ministry of Education and Key Lab of Smart Prevention and Mitigation of Civil Engineering Disasters of the Ministry of Industry and Information Technology, Harbin Institute of Technology, Harbin 150090, China

[4] School of Resources and Environmental Engineering, Inner Mongolia University of Technology, Hohhot 010051, China

[5]Institute of Technical Information for Building Materials Industry（ITIBMI）, Beijing 100024, China

from coastal and saline-alkali areas can penetrate into the interior through concrete pores [2], causing steel corrosion and volume expansion, which in turn leads to concrete cracking and spalling. Meanwhile, the acidic environment formed by urban industrial waste gas and vehicle exhaust accelerates the carbonation process of concrete [3], undermining its protective effect on steel reinforcement, and thereby reducing the durability of the structure. Furthermore, structural fatigue caused by long-term alternating loads leads to the continuous expansion and accumulation of micro-cracks within the concrete, ultimately resulting in a series of defects such as significant cracking, deformation, reduced stiffness, and decreased bearing capacity [4]. If these defects are not reinforced and repaired in a timely and effective manner, they will not only shorten the service life of the project, but also potentially lead to safety accidents such as collapses due to insufficient bearing capacity, resulting in serious casualties, property losses, and even affecting the normal operation of the city and people's livelihood. Therefore, it has become an urgent priority to carry out rapid reinforcement and repair work on concrete structures in the middle and later stages of service, in order to maintain the stable operation of infrastructure and avoid significant safety and economic losses [5].

Facing the aforementioned challenges, during the 13th Five-Year Plan period, China invested a significant amount of funds to renovate over thirty thousand reinforced concrete structures. However, traditional repair materials have become inadequate to meet modern engineering requirements for efficiency, low carbon footprint and durability. With the development of new materials, high-toughness concrete with excellent mechanical properties has been applied in reinforcement engineering, such as ECC, UHPC, and fiber-reinforced polymer (FRP). Research results show that ECC reinforcement materials have excellent bonding performance and good compatibility with concrete structures. Using them for reinforcement can improve the overall ductility, seismic resistance, and energy dissipation performance of concrete structures. However, ECC materials have disadvantages such as high production costs and large cement consumption [6,7]. UHPC possesses ultra-high strength, high toughness, excellent durability, and good bonding performance between new and old interfaces, and has been widely used in the repair of deteriorated concrete components [8-10]. However, its high preparation cost, high carbon emissions, high risks of shrinkage and hydration heat, and inferior ductility compared to ECC limit its large-scale promotion and application. Existing study has shown that FRP is lightweight, high in strength, excellent in corrosion resistance, and convenient to construct [11-13]. However, its exhibit significant performance degradation at high temperatures, high material costs, insufficient interface durability, and are prone to creep under long-term stress. Therefore, there is an urgent need to develop a repair material with high ductility, low cost, and easy construction to meet the current engineering demands.

While advancing this restoration task, another urgent issue that contradicts the “dual carbon” goals has become increasingly prominent, namely the disposal of industrial solid waste [14]. According to the calculation data provided by the Ministry of Housing and Urban-Rural Development, China has a huge amount of solid waste, and its stockpile is estimated to double by 2030. At the same time, the production of industrial solid waste in China continues to grow. According to statistical data from relevant research, the total annual output of five types of solid waste, namely tailings, slag, coal gangue, fly ash, and red mud, has exceeded 3.4 billion tons in 2022, and the utilization rate of solid waste is relatively low. In addition, a large amount of other solid waste will be generated in the industrial production process [15]. The long-term storage of massive solid waste not only occupies valuable land resources, but also releases harmful substances such as heavy metal ions under the action of rainwater, causing secondary environmental disasters including groundwater pollution and soil salinization [16]. The accumulation of industrial solid waste has exerted considerable adverse impacts on society, the economy and the

environment [17]. Considering the urgent pressure of solid waste accumulation and structural repair, processing the industrial solid waste generated and accumulated annually into cementitious materials or aggregates has become a core approach to solving the aforementioned problems [18]. Converting industrial solid waste into construction materials can achieve the dual benefits of environmental protection and turning waste into wealth [19]. Relevant studies have shown that many solid wastes are rich in active cementitious components such as silica and alumina [20], which have the potential to replace cement and aggregates. Using them to prepare new repair materials not only aligns with the national green and low-carbon development strategy, but also yields significant economic benefits.

In this context, researchers have discovered the complementary and synergistic effects of silica fume and fly ash at the levels of physical filling, chemical activity, and hydration kinetics [21]. This can not only significantly improve the mechanical properties and durability of concrete, but also effectively solve key bottleneck problems such as slow early strength development and poor volume stability when using a single admixture. However, the total solid waste content is low, and it will significantly reduce the material fluidity. Lu et al. [22] proposed a synergistic modification method for foam concrete incorporating industrial waste stone powder and nano-GO, which significantly improved water absorption performance while enhancing mechanical properties, and verified its favorable engineering applicability through field tests. However, their research object is lightweight subgrade filler, which can hardly meet the high toughness requirements for structural repair. Song et al. [23] extracted geopolymer foam concrete from industrial solid waste and conducted experiments to investigate the impact of geopolymer foam concrete performance on solid waste such as coal gangue. They found that the performance of geopolymer foam concrete directly extracted from solid waste materials was poor, and better performance could only be achieved by combining it with other materials, with the proportion of solid waste not exceeding 50%. Du et al. [24] further revealed through microscopic characterization that the calcium silicate hydrate (C-S-H) gel formed in the multi-component solid waste system has a denser microstructure, thereby significantly enhancing the erosion resistance of the matrix. However, the test design ratio is relatively limited, and the $CaO/CaSO_4$ ratio needs further refinement. Luo et al. [25] attempted to introduce ternary mixed fly ash, methanol lignin, and slag into reinforced composites, verifying the regulatory effect of solid waste components on the material's workability. However, their component design was relatively limited, and the optimal mix proportion would change when adjusting the component content. Li et al. [26] studied industrial solid waste permeable concrete (ISWPC) based on a novel alkali-activated ternary binder (A-CGSB) and coal gangue (CG) aggregates. The results showed that the performance of ISWPC critically depends on the water-to-binder (W/B) ratio. Low ratio hinders uniform coating and leads to a decrease in strength. A high ratio leads to slurry settling and destroys permeability, but the total solid waste rate of this study was only 25%. In summary, most of the high-solid waste-based repair materials currently prepared struggle to balance high solid waste content with excellent mechanical and deformation properties. When increasing the amount of solid waste to achieve environmental and low-cost goals, it often leads to a decrease in material strength, insufficient ductility, and weakened crack control ability. When pursuing good mechanical and deformation performance, it is necessary to reduce the amount of solid waste, which violates the concept of green and low-carbon. This inherent contradiction seriously restricts the engineering promotion and green transformation process of high solid waste based repair materials. When increasing the amount of solid waste to achieve environmental protection and low-cost goals, it will lead to a decrease in material strength, insufficient ductility, and weakened crack control ability. When pursuing good mechanical and deformation performance, it is necessary to reduce the amount of solid waste, which violates the concept

of green and low-carbon. This inherent contradiction seriously restricts the engineering promotion and green transformation process of high solid waste based repair materials.

In view of this, this study used blast furnace slag (BFS) and waste glass powder (WGP) as cement replacement components, constructed a multi-component solid waste composite cementitious system through gradient content regulation, and introduced PE fibers, steel fibers, and PP fibers to prepare multi-scale ternary hybrid fiber-reinforced composites. The evolution laws of the material's workability, mechanical strength characteristics, and tensile deformation performance were systematically explored. With the aid of multi-dimensional microscopic characterization techniques such as X-ray diffractometer (XRD), thermogravimetric analyzer (TG-DTG), and scanning electron microscope (SEM), the multi-component interface coupling effect and the microstructure evolution mechanism were systematically revealed. A theoretical model of material stress-strain evolution was proposed, which clarified the inherent mechanism of hybrid fiber synergistic reinforcement and the material's mechanical behavior, laying a solid theoretical foundation for the research and development and performance optimization of low-carbon, high-solid-waste-content engineering repair materials.

2 Materials and methods

2.1 Raw materials

In this study, the cementitious materials selected include M32.5 cement, S95 grade blast furnace slag (BFS), and waste glass powder (WGP). Their oxide compositions are presented in Table 1, while the particle size distribution and microstructure are illustrated in Fig. 1 and 2, respectively.

Table 1. Chemical composition of cementitious materials

Cementitious material	Chemical composition (%)								
	SiO_2	Al_2O_3	CaO	Fe_2O_3	MgO	SO_3	TiO_2	K_2O	Others
Cement	26.39	18.15	45.92	2.59	2.03	3.13	0.76	0.76	0.27
BFS	33.21	15.76	37.14	0.71	8.51	2.71	1.91	-	0.05
WGP	66.44	20.52	8.19	0.05	1.76	0.03	0.06	0.06	2.89

From the particle size distribution curve, it can be observed that the peak volume percentages of WGP and BFS occur in the 10-20 μm range, whereas the peak for cement tends towards 30 μm. The cumulative volume curve further confirms that cement has the lowest proportion of fine particles. As can be seen from Fig. 2, BFS primarily consists of irregularly shaped particles that are finer and have a denser surface. The active glassy structure with a high specific surface area can optimize particle gradation and promote the pozzolanic effect in alkaline environments. WGP exhibits a dense lamellar structure with a relatively smooth surface, capable of undergoing secondary hydration in alkaline environments to enhance the performance of the interfacial transition zone. The fine aggregate is composed of quartz sand with a mesh size ranging from 80 to 120. To improve the machinability of the composite material, polycarboxylic acid superplasticizer was incorporated. To enhance the mechanical properties and ductility of HWRM, multi-scale hybrid fibers were incorporated, specifically including 12 mm PE fibers, 3 mm PP fibers, and 6 mm steel fibers. The main technical parameters of the three types of fibers are presented in Table 2.

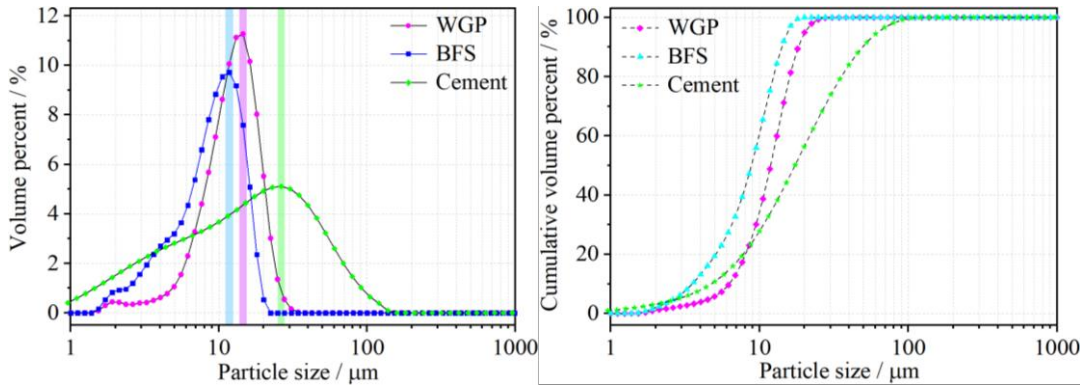


Fig.1. Particle size distribution of cementitious materials

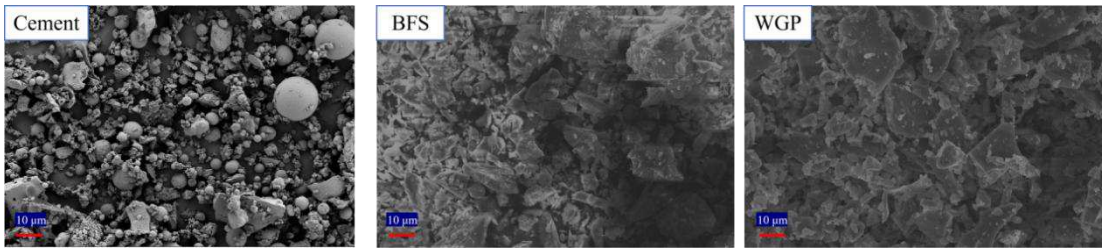


Fig.2. Microscopic morphology of cementitious materials

Table 2. Main technical parameters of fiber

Fiber	Diameter /μm	Density g/cm^3	Length /mm	Breaking modulus/GPa	Breaking strength /MPa
PE	24	0.98	12	116	3000
PP	30	0.91	3	40	1600
Steel	200	7.8	6	200	2906

2.2 Mix Proportion

This study designed a total of 14 mix proportions, with a focus on the influence of BFS and WGP substitution rates, as well as the volume fraction ratio of ternary hybrid fibers. Among them, $B_0W_0PE_2$ was set as the control group. The water-binder ratio and sand-binder ratio were set at 0.28 and 0.45, respectively. Table 3 presents the mix proportions of HWRM. The numerical values following cement, BFS, and WGP in Table 3 represent the mass fraction of each raw material in the total cementitious material, while the numerical values following PE fiber, Steel fiber, and PP fiber represent the volume fraction of the fibers.

Table 3. Mix proportion (%)

Number	Cement	BFS	WGP	PE fiber	Steel fiber	PP fiber
$B_0W_0PE_2$	100	0	0	2	0	0
$B_{10}W_0PE_2$	90	10	0	2	0	0
$B_{30}W_0PE_2$	70	30	0	2	0	0
$B_{50}W_0PE_2$	50	50	0	2	0	0
$B_{70}W_0PE_2$	30	70	0	2	0	0
$B_{45}W_{10}PE_2$	45	45	10	2	0	0
$B_{40}W_{20}PE_2$	40	40	20	2	0	0
$B_{35}W_{30}PE_2$	35	35	30	2	0	0
$E_{1.5}S_{0.25}P_{0.25}$	45	45	10	1.5	0.25	0.25

$E_{1.5}S_{0.5}P_0$	45	45	10	1.5	0.5	0
$E_{1.5}S_0P_{0.5}$	45	45	10	1.5	0	0.5
$E_1S_{0.75}P_{0.25}$	45	45	10	1	0.75	0.25
$E_1S_{0.25}P_{0.75}$	45	45	10	1	0.25	0.75
$E_1S_{0.5}P_{0.5}$	45	45	10	1	0.5	0.5

2.3 Test method

2.3.1 Preparation process

Fig. 3 illustrates the preparation process of HWRM. Firstly, cement, BFS, and WGP were mixed together in a mixing pot and stirred at low speed for 1 min. Then, added pre-weighed quartz sand and continue stirred at low speed for another 1 min. When the cementitious material and fine aggregate were mixed evenly, water and water reducing agent were added to the mixture. The mixture was first stirred at low speed for 1 min, and then stirred at high speed for 1.5 min. Finally, pre-dispersed fibers were added, and the mixture was stirred at low speed for 2 minutes, followed by high-speed stirring for another 2 minutes until the slurry was evenly mixed. Afterwards, the slurry was poured into different types of molds, vibrated, covered and cured for 24 hours, demolded, and placed in a standard curing room (relative humidity ≥ 90%, temperature 20±1 ℃) for 28 days of curing. Fig. 3 shows the preparation process of HWRM.

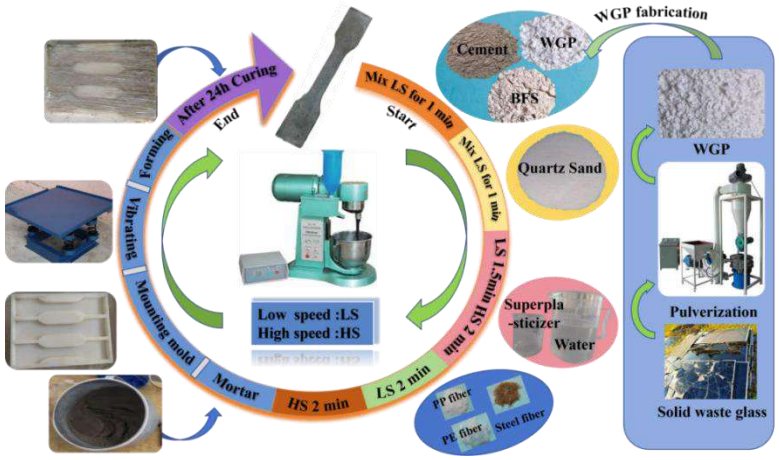


Fig.3. The preparation process of HWRM

2.3.2 Fluidity

The fluidity test was conducted in accordance with the GB/T 2419-2005 (Chinese standard) [27]. The prepared HWRM was placed into a test mold with a height of 60±0.5 mm, an upper inner diameter of 70±0.5 mm, and a lower inner diameter of 100±0.5 mm. The first 2/3 of the mold was filled with HWRM, and a scraper was used to scratch it 5 times in two mutually perpendicular directions. A tamper was then used to press from the edge to the center 15 times. The HWRM was further filled into the mold until it protrudes about 20 mm above the mold. Use a pestle to press from the edge to the center 10 times. The mold sleeve was removed, and a trowel was used to smooth the surface. The test mold was lifted vertically, and the jigging table was immediately started. After the 25 th jump, the maximum diameters of the HWRM bottom surface in two perpendicular directions were measured, and their average was taken as the fluidity.

2.3.3 Flexural strength

The flexural performance was tested in accordance with the GB/T 17671-2021 (Chinese standard) [28], with a specimen size of 40 mm×40 mm×160 mm. Place one side of the specimen on the press machine, with a loading rate of 50 N/s. The calculation method for flexural strength is shown in Eq.(1).

$$R_{\mathrm{f}} = \frac{1.5F_f S}{b^3} \tag{1}$$

where, R_{f} represents the flexural strength of the specimen (MPa); F_{f} denotes the load borne by the specimen (N); S is the span between the supports (mm); b is the side length of the square cross-section of the prism (mm).

2.3.4 Compressive strength

The compressive strength was determined according to the "ISO method for testing the strength of cement mortar" (GB/T 17671-2021), using specimens after flexural testing with a cross-section of 40 mm×40 mm. The loading rate for the compressive test was 2.4 kN/s. The calculation method for compressive strength is shown in Eq.(2).

$$R_{\mathrm{c}} = \frac{F_{\mathrm{c}}}{A} \tag{2}$$

where, R_c represents the compressive strength of the test specimen (MPa); F_c denotes the maximum load applied when the test specimen fails (N); A is the compressed area (mm^2).

2.3.5 Uniaxial tensile performance

The uniaxial tensile performance were tested in accordance with the Japanese recommended standard “Recommendations for Design and Construction of HPFRCC” [29], with specimen dimensions of 330 mm×60 mm×13 mm. The loading process was controlled by displacement, with a loading rate of 0.1 mm/min. The calculation methods for stress and strain are shown in Eqs. (3)~(4).

$$\sigma = \frac{F_{\mathrm{t}}}{A_{\mathrm{t}}} \tag{3}$$

$$\varepsilon = \frac{\Delta l}{l} \tag{4}$$

where, σ represents uniaxial tensile stress (MPa); F_{t} denotes tensile force (N); A_{t} is the cross-sectional area of the specimen (mm^2); ε is the ultimate tensile strain (%); Δl is the deformation amount; l represents the length of the tensile section.

2.3.6 X-ray diffraction (XRD)

The XRD of some test specimens was tested using the DX-2700BH from Dandong Haoyuan. The central fragment of the test specimen was placed in anhydrous ethanol to terminate its hydration. Before testing, the sample was dried in an oven at 40 °C for 24 h, then ground and sieved through a 200-mesh sieve. Then conduct XRD testing on the sample, with a scanning range of 5° to 90°.

2.3.7 Thermogravimetric (DTG-TG)

The heat changes and mass loss of the sample were tested using a Hitachi STA7300 synchronous thermal analyzer, following the same sample preparation process as for XRD. Weighed 5-10 mg of HWRM powder into an alumina crucible and recorded the real-time curve of sample mass change with temperature. The temperature was increased from 30 ℃ to 1000 ℃ at a constant heating rate of 10 ℃/min, and the test was conducted under a nitrogen atmosphere.

2.3.8 Scanning electron microscopy (SEM)

The micro-morphology of the sample was tested using a Thermo Fisher Axia ChemiSEM electron

microscope. A fragment from the middle part of the specimen was taken as the SEM test sample. After vacuum drying, gold spraying was performed on the sample surface to improve conductivity. According to the analysis requirements, some magnifications were selected to observe the pore structure and product morphology of the sample.

3 Test results and analysis

3.1 Fluidity

The test results of the HWRM fluidity are presented in Fig. 4. with a fluidity that ranged from 215 to 280 mm. From the figure, it can be seen that the addition of BFS, steel fibers, and PP fibers significantly improved the fluidity of the slurry, while WGP had a certain degree of negative impact on fluidity. When BFS gradually replaced cement, the fluidity was improved by 15.9%-57.2%. This was mainly because cement has higher reactivity than BFS, and the incorporation of BFS slows down the hydration process of HWRM, thereby optimizing the paste structure and releasing more free water, which led to an increase in the fluidity of HWRM. After WGP was added, the fluidity of the slurry first decreased and then increased with the increase of WGP substitution rate, with the fluidity ranged from 198 to 220 mm. However, it was 36.6%–51.7% higher than that of the control group ECC. This result indicated that incorporating an appropriate amount of WGP can significantly improve the fluidity of the slurry, making it excellent for construction applications. At the same time, it was indicated that at low concentrations, the flaky WGP particles tend to overlap with each other, slightly hindering the fluidity of the slurry. At the same time, it indicates that the sheet-like WGP particles are prone to overlap with each other at low dosages, slightly hindering the fluidity of the slurry. However, as the concentration increases, the smooth flaky WGP particles exhibit a significant lubricating and directional arrangement effect, effectively reducing the frictional resistance between particles [30], thereby greatly improving the fluidity of the slurry.

When the replacement ratio of BFS and WGP was 55%–65%, the fluidity of HWRM ranged from 227 to 269 mm. The addition of 3 mm PP fibers and 6 mm steel fibers had a positive impact on fluidity [31,32]. This was mainly because PE fibers have a relatively large aspect ratio, which tends to entangle with each other in the slurry, increasing the internal structural resistance of the slurry [33]. However, PP fibers and steel fibers possessed smooth surfaces, which allowed them to disperse more easily and reduced the frictional resistance between particles. Therefore, under the same total dosage, the replacement of PE fibers with PP fibers and steel fibers effectively improved the fluidity of the slurry and delivered superior workability [34]. When the substitution rate of both PP fibers and steel fibers was 0.5%, the fluidity of HWRM reached its maximum, an increase of 35.86% compared to the control group.

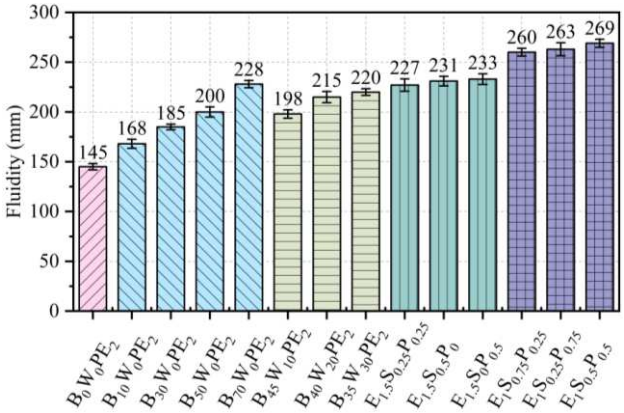
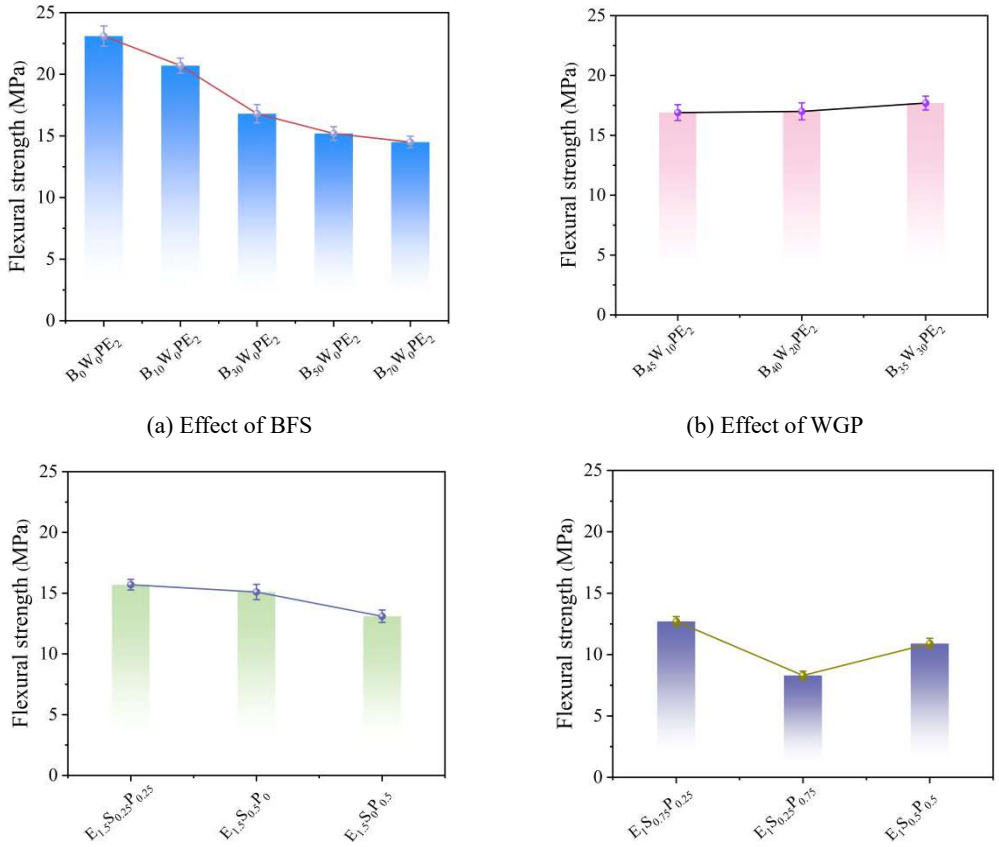


Fig.4. Fluidity test results of HWRM

3.2 Flexural strength

The 28 d flexural strength results of HWRM are illustrated in Fig.5, with values ranged from 8.3 to 23.1 MPa. As can be seen from the figure, BFS addition exerted an obvious negative effect on the flexural strength of HWRM, causing a strength reduction of 10.4% to 37.2%. Mainly because the proportion of highly active clinker minerals in the cementitious system continues to decrease with the increase of BFS substitution rate, and the overall hydration reaction process is inhibited [35]. Although the presence of BFS causes secondary hydration effect in the slurry, the hydration process within 28 d was limited, so the flexural strength gradually decreased with the increase of BFS content. After adding WGP, the flexural strength of HWRM slightly increased. This is because WGP can improve the interface transition zone between the slurry and the aggregate, and effectively suppress the initiation and propagation of cracks under bending stress [36].

Further comparison revealed that the flexural strength of HWRM decreased to varying degrees when steel fibers and PP fibers replaced some PE fibers. When the content of PE fibers was 1.5% and the content of both steel fibers and PP fibers was 0.25%, the flexural strength decreased by 7.1%. This is mainly because PE fibers have good interfacial compatibility and bonding properties with the slurry, which can effectively bridge cracks under bending loads, inhibit crack initiation and propagation, and fully exert their toughening and crack-resistance effects [37]. As expected, under the condition of the same substitution rate of PP fiber and steel fiber, the flexural strength decay rate of HWRM was faster when PP fiber was used to replace PE fiber. Mainly because compared with steel fibers, PP fibers have lower length and elastic modulus, poorer bonding effect with the matrix, and are difficult to effectively bear loads and suppress crack propagation at the same substitution rate. Therefore, their effect on improving the flexural strength of HWRM is far inferior to that of steel fibers. This explanation has been confirmed in the study [38].



(a) Effect of BFS

(b) Effect of WGP

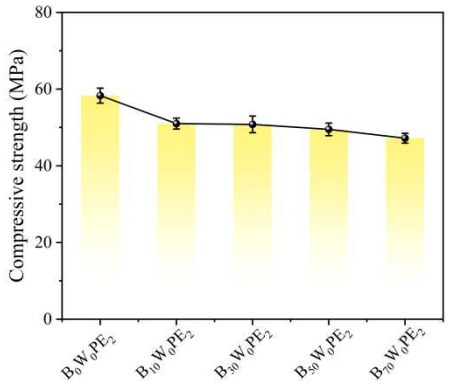
(c) PE fiber content of 1.5% (d) PE fiber content of 1.0%

Fig. 5. The flexural strength test results of HWRM

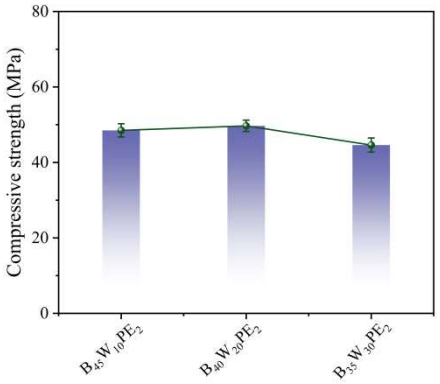
3.3 Compressive strength

Fig. 6 shows the compressive strength test results of HWRM at 28 d, with a compressive strength ranged from 36.7-58.3 MPa. As can be seen from the figure, BFS exerted a negative effect on the compressive strength of HWRM, resulting in a reduction of 12.5% to 19% relative to the cement matrix. After adding WGP, the compressive strength of HWRM was improved to varying degrees. When the content of WGP was controlled within 20%, the compressive strength could be maintained around the benchmark group level. Nevertheless, when the WGP content reached 30%, the compressive strength of HWRM declined markedly, with a decrease of 9.9% compared with the control group ECC. This result indicated that excessive WGP content would exert adverse effects on the compressive strength of HWRM. Therefore, if pursuing high-strength materials, it is recommended to control the substitution rate of WGP within 20%.

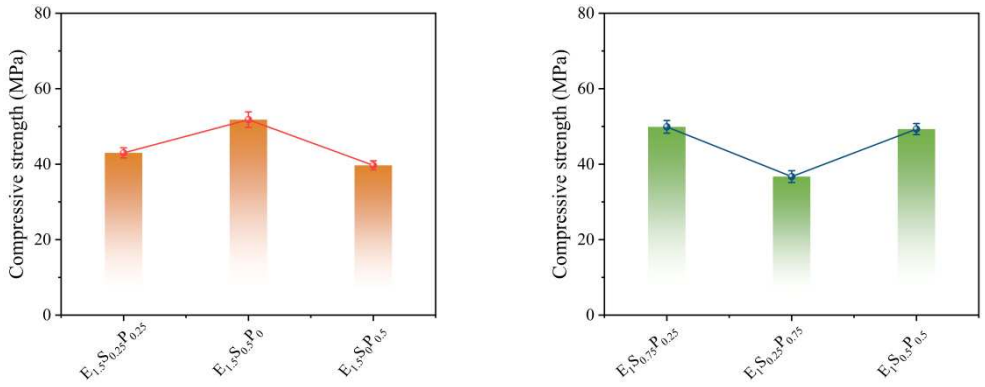
When the PE fiber content was 1.5% and the steel fiber replacement ratio was 0.5%, the compressive strength of HWRM was higher than that of the control group, which was different from the flexural strength performance. The main reason for this phenomenon is that an appropriate amount of steel fiber can effectively restrain the lateral deformation of the matrix under compression [39], inhibit the development of microcracks, and thus exert a positive effect on the compressive strength of HWRM. However, under flexural loading, replacing part of the PE fibers with steel fibers weakened the overall fiber bridging effect and toughness contribution, leading to a decrease in flexural strength. When the PE fiber content was 1%, the trend of compressive strength changing with the fiber replacement ratio was consistent with that of flexural strength. It can be seen that different fiber components have significant differences in their effects on the flexural strength and compressive strength of HWRM. In practical applications, various mechanical properties should be comprehensively considered, and the selection of fiber types and ratios should be reasonable.



(a) Effect of BFS



(b) Effect of WGP



(c) PE fiber content of 1.5% (d) PE fiber content of 1.0%

Fig.6. The compressive strength test results of HWRM

3.4 Uniaxial tensile stress-strain

Fig. 7 shows the uniaxial tensile stress-strain curve of HWRM at 28 d. As shown in the figure, the stress-strain curves of all HWRMs can be roughly divided into three stages: elastic stage, strain hardening stage, and strain softening stage. The stress-strain curves revealed that when the steel fiber content was high, the strain hardening phase of HWRM was less pronounced, while the strain softening phase became more prominent, which is similar to the results obtained by Cao et al. [40]. The primary reason for this phenomenon is that the elastic modulus of steel fibers is significantly higher than that of the matrix. After initial cracking, stress rapidly localized on a single main crack, and the fibers primarily engaged in single-crack bridging and energy dissipation through pulling, which failed to satisfy the condition for uniform stress dispersion during multi-crack propagation [41]. Additionally, it could be observed that the stress-strain curves of HWRM exhibited serrated fluctuations, which is primarily due to the combined effects of new cracks continuously emerging in the matrix and fibers repeatedly bridging and re-bearing the load. This visually reflects the toughening and crack-resistance mechanisms of fibers [42].

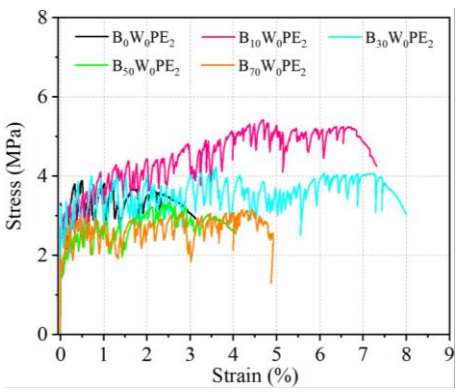
As can be seen from Fig. 7(a), the ultimate stress and ultimate strain of the cement composite material were 3.5 MPa and 2.4%, respectively. After substituting a portion of cement with BFS, the ultimate strain of HWRM was significantly improved, reaching up to 7.4%. Compared to pure cement composite materials, it has improved by 208%, demonstrating superior tensile deformation performance and simultaneous increase in ultimate tensile strength. When the BFS content was increased to 50% to 70%, the tensile performance of HWRM decreased, with the ultimate stress dropping to 3 MPa and the ultimate strain being 3.5% and 4.6%, respectively. However, they were still higher than those of the control specimen $B_0W_0PE_2$. This is mainly attributed to the fact that an appropriate amount of BFS can optimize the microstructure of the matrix, improve the interface transition zone, and enhance homogeneity [43], while an excessive amount of BFS can lead to insufficient hydration, thereby reducing the matrix strength and bearing capacity.

As can be seen from Fig.5(b), the addition of WGP had varying degrees of impact on the uniaxial tensile ultimate stress and strain of HWRM. When the WGP content was 10% and 20%, respectively, the ultimate tensile stress of HWRM was improved compared to the control group, but the ultimate strain decreased by 8.57% to 31.43%. This is because the incorporation of a certain amount of WGP densifies the matrix through micro-aggregate filling and pozzolanic effect [44], resulting in an increase in uniaxial tensile stress. However, the increase in compactness and elastic modulus leads to increased material brittleness and a decrease in ultimate strain. When the WGP replacement ratio increased to 30%, the

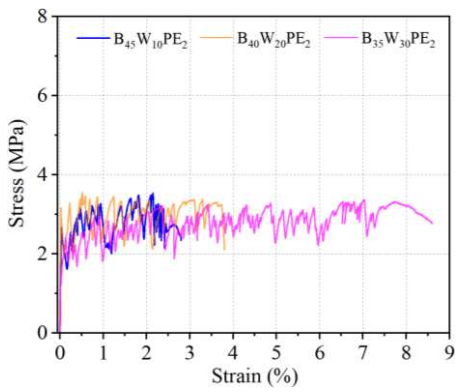
uniaxial tensile strain of HWRM increased significantly. This is mainly because secondary hydration effectively improves the interface transition zone, inhibits rapid crack propagation, and results in a more uniform stress distribution within the matrix. The tensile cracks developed in a dispersed manner and energy was dissipated, leading to a significant increase in ultimate strain. It is worth noting that the solid waste replacement ratio at this point was as high as 65%.

As can be seen from Fig.5(c), after replacing a portion of PE fibers with steel fibers and PP fibers, the ultimate stress of HWRM increased, but the tensile strain was affected to varying degrees. The increase in ultimate stress was attributed to the formation of a denser and more uniform fiber network within the slurry by an appropriate amount of short fibers [45], which effectively compensated for the uneven distribution and insufficient overlap of long fibers in local areas. At the same time, the composite hybrid effect of steel fibers and PP fibers further optimizes the synergistic working performance of the fiber system, enhancing the overall toughening and strengthening effect. When replacing PE fibers with 0.5% steel fibers alone, the ultimate tensile strain of HWRM was 2.11%, which is mainly attributed to the high stiffness and elastic modulus of steel fibers, which strongly constrain the deformation of the matrix and significantly reduce the tensile strain of the specimen, weakening the strain hardening characteristics. When steel fibers and PP fibers are replaced by 0.25% composite or 0.5% PP fibers alone, PP fibers have high elongation [46] and strong deformation ability, which can form a synergistic toughening effect with steel fibers and alleviate the rigid constraints brought by high modulus fibers, making crack development more uniform and energy dissipation more sufficient. Therefore, the tensile strain was significantly improved, and the strain hardening performance was significantly improved.

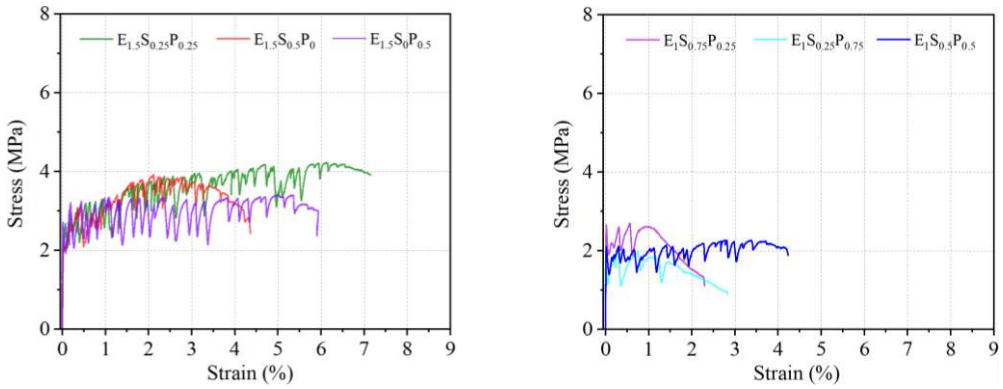
As can be seen from Fig.5(d), when 50% of the PE fibers were replaced, the overall tensile performance of HWRM was unsatisfactory. When both the PP fiber content and steel fiber content were 0.5%, the ultimate tensile strain of HWRM was 3.7%. When the PP fiber content was increased to 0.75%, both the ultimate tensile stress and strain of HWRM decreased significantly. This is mainly due to the insufficient content of steel fibers and PE fibers, resulting in weakened reinforcement and bridging effects. However, PP fibers have poor adhesion, and the introduction of a large number of low elastic modulus PP fibers creates more weak interfaces, which weakens the mechanical properties and stress transfer efficiency of the matrix. When the steel fiber content was increased to 0.75%, the tensile stress of HWRM decreased slightly, while the tensile strain decreased significantly. This is because steel fibers with high elastic modulus effectively enhance the load-bearing capacity, but the steel fibers themselves have a low elongation rate and are prone to instantaneous overall pullout after bond failure with the matrix. Their energy dissipation efficiency is much lower than that of PE fibers, thus leading to a significant reduction in the deformation capacity of HWRM.



(a) Effect of BFS



(b) Effect of WGP



(c) PE fiber content of 1.5% (d) PE fiber content of 1.0%

Fig.7. Results of uniaxial tensile test for HWRM

3.5 X-ray diffraction (XRD)

Fig. 8 shows the XRD test results of HWRM at 28 d. As can be seen from the figure, characteristic diffraction peaks of $Ca(OH)_2$, $CaCO_3$, SiO_2, C_2S, and C_3S were detected in the phase composition of all three groups of specimens. Among them, the peak at $2\theta \approx 29.3°$ corresponded to the overlapping diffraction peaks of $CaCO_3$ and C_3S [47]. Specimen $B_{45}W_{10}PE_2$ exhibited the highest peak intensity at this position, followed by $B_{10}W_0PE_2$, while specimen $B_0W_0PE_2$ displayed the lowest diffraction peak intensity. The diffraction peaks of $Ca(OH)_2$ were mainly distributed at $2\theta \approx 18.1°$ and 34.0°. The $Ca(OH)_2$ peak intensity was the highest for $B_0W_0PE_2$, and gradually decreased in the order of $B_{10}W_0PE_2$ and $B_{45}W_{10}PE_2$. This indicated that the pozzolanic reaction of solid waste continuously consumed $Ca(OH)_2$ in the system [48], and the higher the solid waste content, the more remarkable the consumption. The diffraction peaks of C_2S were located at $2\theta \approx 32.5°$ and 41.0°. Specimen $B_0W_0PE_2$ showed the most prominent peak intensity, and the peak intensity gradually diminished after solid waste incorporation. The diffraction peak of SiO_2 is located near $2\theta \approx 26.6°$[49], and the diffraction peak intensity of specimen $B_{45}W_{10}PE_2$ was significantly higher than the other two groups of specimens. Mainly because WGP contains a large amount of SiO_2, the study by Dueramae et al. [50] provides direct evidence for this explanation.

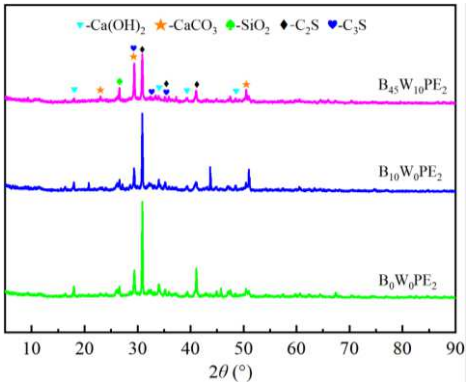


Fig.8. XRD pattern of HWRM at 28 d

3.6 Thermogravimetric analysis (DTG-TG)

Fig. 9 shows the DTG-TG test results of HWRM at 28 d. From the TG curve, it can be observed that all specimens underwent three main stages of mass loss during heating from room temperature to

1000 °C, which corresponded to the three primary weight loss peaks on the DTG curve. The first stage occurred at approximately 110 °C, where the TG curve presented a slow descending trend, corresponding to a relatively weak weight loss peak on the DTG curve. This stage is mainly attributed to the evaporation of free water inside specimens and the dehydration of C-S-H gel [51], resulting in a low mass loss ratio. The second stage occurred between 400–450 °C, during which the descending rate of the TG curve accelerated, corresponding to a distinct weight loss peak on the DTG curve. This stage is primarily caused by the thermal decomposition of $Ca(OH)_2$ hydration products. The mass loss magnitude directly reflects the hydration degree of cementitious materials and the stability of hydration products. The third stage occurred within 600–800 °C, where the TG curve exhibited a sharp decline, corresponding to the most prominent weight loss peak on the DTG curve. This stage is mainly the decomposition of calcium carbonate, which is the main cause of mass loss [52]. Its decomposition temperature and rate are closely related to the crystal form and content.

By comparing the DTG-TG curve differences among various specimens, it can be observed that specimen $B_0W_0PE_2$ exhibited a high hydration degree, accompanied by the highest contents of generated $Ca(OH)_2$ and carbonated $CaCO_3$. Therefore, the maximum weight loss was observed in the high temperature range of 600-800 ℃, and the DTG decomposition peak was the sharpest, indicating that the hydration product had a dense structure, high crystallinity, and good thermal stability, which is consistent with the macroscopic mechanical trend. With the gradual increase in the replacement ratios of BFS and WGP, calcium hydroxide in the system was continuously consumed by secondary hydration, which correspondingly reduced the production of calcium carbonate. The weight loss gradually decreases in the high temperature range on the TG curve, and the overall DTG peak shape becomes wider and smoother, indicating a decrease in the regularity and structural density of hydration products. Therefore, the DTG-TG test results can provide favorable evidence for the macroscopic performance changes of HWRM.

The TG-DTG quantitative analysis results showed that different solid waste replacement ratios had a significant effect on the hydration reaction of the system [53]. It was found that specimen $B_{10}W_0PE_2$ had the highest bound water content and the lowest $Ca(OH)_2$ content, indicating that the addition of an appropriate amount of BFS promoted the secondary hydration reaction, consumed part of $Ca(OH)_2$ and formed more hydrated C-S-H gel. With the gradual increase of the solid waste replacement ratio, the bound water contents of $B_{50}W_0PE_2$ and $B_{45}W_{10}PE_2$ decreased, while the $Ca(OH)_2$ contents increased correspondingly. This indicated that within the test curing age, the latent activities of BFS and WGP could not be fully brought into play, the generation of hydration products was restricted, and partial $Ca(OH)_2$ was not fully consumed. The mass loss results in the 580–780 °C range showed that there were certain differences in carbonate content among all groups, which was mainly related to the carbonates in raw materials and the carbonation reaction of hardened pastes, and could assist in reflecting the carbonation characteristics of the system [53,54]. It was concluded from this that an appropriate solid waste replacement ratio was beneficial to promoting the secondary hydration reaction, while a higher replacement ratio might lead to a decrease in the amount of hydration products due to insufficient reaction degree, which was consistent with the variation trend of compressive strength.

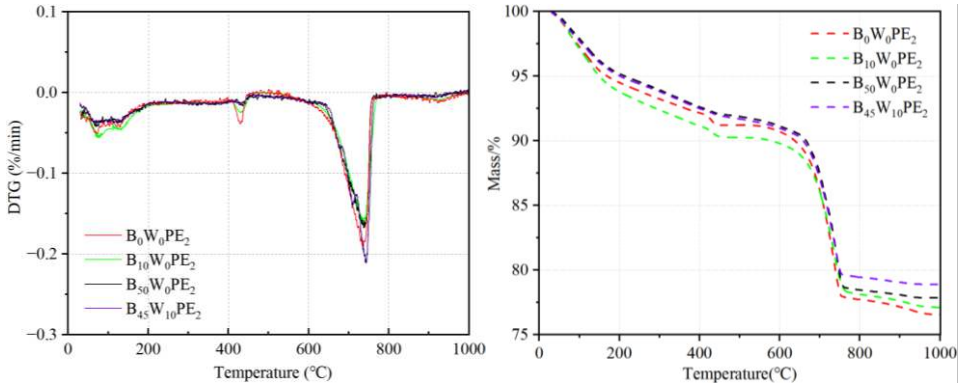


Fig.9. DTG-TG of HWRM at 28 d

3.7 Scanning electron microscopy (SEM)

Fig. 10 shows the SEM test results of HWRM at 28 d. $B_0W_0PE_2$ matrix of the specimen was mainly interlaced and lapped by flocculent and reticular C-S-H gel, while hexagonal tabular $Ca(OH)_2$ crystals and a small amount of acicular ettringite AFt crystals existed. These hydration products collectively bond unhydrated particles and inert fine aggregates together. This phenomenon provides a good explanation for the high strength performance of cement composite materials.

Specimen $B_{30}W_0PE_2$ contained PE fibers embedded in the HWRM matrix, with fiber surfaces tightly coated by C-S-H gels. The fibers exerted a bridging effect to restrain crack propagation under tensile loading, thereby laying a favorable structural foundation for the high tensile strain capacity of the composite. A small amount of flocculent hydration product C-S-H gel was attached to the surface of PE fiber inside the specimen $B_{35}W_{30}PE_2$, and there were microcracks and debonding at the interface between the fiber and the matrix. Therefore, when the specimen is in a tensile state, the PE fibers dissipate the crack propagation ability through interface debonding, sliding, and bridging, promoting the material to withstand greater deformation. From the microstructure of specimen $B_{50}W_0PE_2$, it can be seen that after replacing 50% with BFS, the hydration products inside the specimen become loose and porous, with poor structural density and a large number of unhydrated particles. This phenomenon provides favorable evidence for the insufficient macroscopic performance of the specimen. From the internal structure of specimen $E_1S_{0.75}P_{0.25}$, it can be seen that PE fibers were interlaced with steel fibers, and some fibers had hydration products attached to their surfaces, with traces of steel fibers being pulled out of the matrix. Further analysis showed that the skeleton support and interlocking effect of steel fibers effectively strengthened the compressive bearing capacity of the matrix, resulting in an increase in the compressive strength of the specimens. However, their own deformation performance was poor and they may produce hole defects after being pulled out, leading to a significant decrease in the tensile capacity of $E_1S_{0.75}P_{0.25}$.

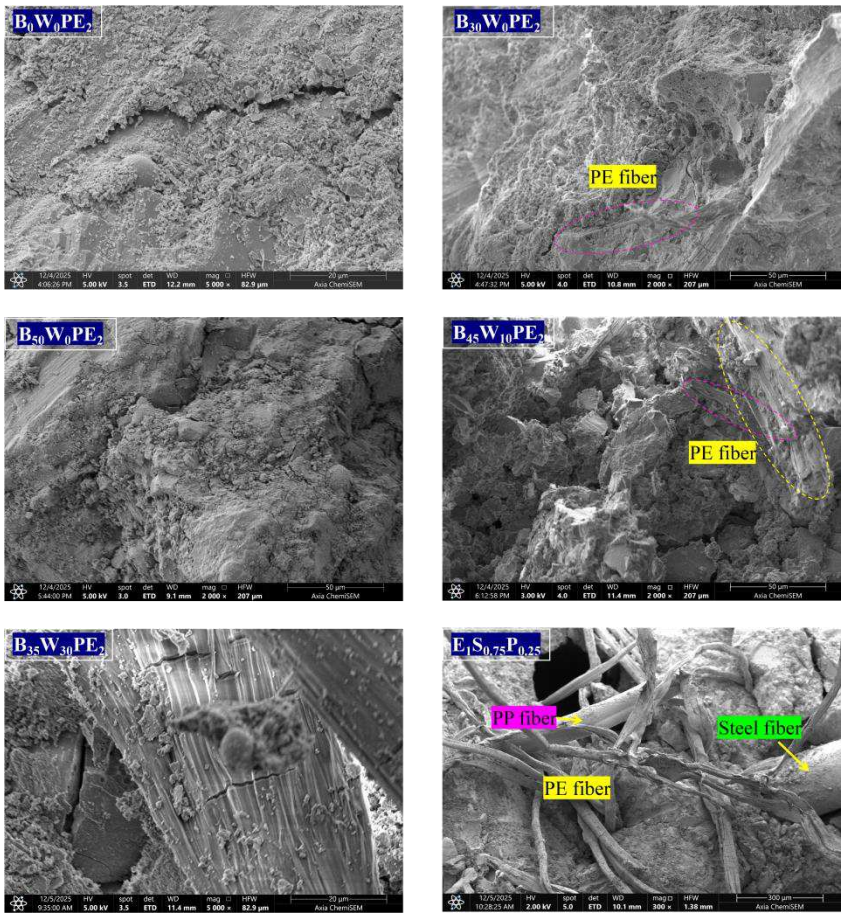


Fig. 10. Microscopic morphology of HWRM

4 Theoretical analysis of stress-strain curve

4.1 Establishment of theoretical model

To promote the engineering application and structural safety design of HWRM, this study predicted its uniaxial tensile constitutive relationship. The test results indicated that the tensile stress-strain behavior of the multi-scale hybrid fiber system without steel fibers exhibited typical strain hardening characteristics and can be simplified into a dual line model. However, after the incorporation of steel fibers, HWRM exhibited a significant strain softening phase after the ultimate load, which is directly related to the synergistic reinforcement effect between hybrid fibers. Therefore, it is necessary to introduce a softening segment based on the dual line model, expanding the constitutive model to a three-stage model to fully cover the full-range mechanical behavior of the material, from linear elasticity, strain hardening to softening failure [55].

From this, it can be inferred that the uniaxial tensile constitutive relationship of HWRM without steel fibers is described by a dual line model. The first stage is the linear elastic stage, where stress and strain increase linearly, and the material is in an elastic deformation state. This stage terminates at the cracking point. The second stage continues to rise linearly from the cracking point until the ultimate stress is reached. After the incorporation of steel fibers, HWRM follows a three-stage constitutive model, with a new strain softening stage added after the peak stress, where stress gradually decreases as strain increases. The uniaxial tensile constitutive relationship of HWRM can be expressed by the following Eqs.

$$\sigma(\varepsilon)=\begin{cases} E_{\mathrm{c}}\varepsilon & 0\le\varepsilon\le\dfrac{\sigma_{\mathrm{ss}}}{E_{\mathrm{c}}} \\ \sigma_{\mathrm{ss}}+\alpha_1\left(\varepsilon-\dfrac{\sigma_{\mathrm{ss}}}{E_{\mathrm{c}}}\right) & \dfrac{\sigma_{\mathrm{ss}}}{E_{\mathrm{c}}}<\varepsilon\le\varepsilon_{\mathrm{cu}} \\ \alpha_2\sigma_{\mathrm{cu}} & \varepsilon>\varepsilon_{\mathrm{cu}} \end{cases} \tag{5}$$

$$\alpha_1=\frac{\sigma_{\mathrm{cu}}-\sigma_{\mathrm{ss}}}{\varepsilon_{\mathrm{cu}}-\sigma_{\mathrm{ss}}/E_{\mathrm{c}}} \tag{6}$$

$$\alpha_2=\left(\frac{\varepsilon_{\mathrm{cu}}}{\varepsilon}\right)^{\frac{2}{I_{R_v}}} \tag{7}$$

$$I_{R_v}=\xi_3\sum_{i=1}^{n}\beta_i V_i\frac{l_i}{d_i}\left(\frac{E_i}{E_{\mathrm{sf}}}\right)^{r_i} \tag{8}$$

where, σ_{ss} is the initial cracking stress; σ_{cu} is the ultimate stress; $\varepsilon_{\mathrm{cu}}$ is the ultimate strain; E_{c} is the elastic modulus of HWRM; α_1 is the reinforcement coefficient; α_2 is the softening coefficient; I_{R_v} is the fiber reinforcement factor [56]. Since this study adopts a ternary hybrid fiber system consisting of PE fiber, steel fiber, and PP fiber, the value of n is 3. ξ_3 is comprehensive correction factor considering the influence of solid waste substitution rate and ternary fiber hybrid system; β_i is the fiber interfacial bonding coefficient; r_i is the fiber characteristic coefficient. V_{i} is the volume fraction of the i-th fiber; l_i is the length of the i-th fiber; d_i is the diameter of the i-th fiber; E_i is the elastic modulus of the i-th type of fiber; E_{sf} is the elastic modulus of steel fibers.

According to the study by Li et al. [57], the stable cracking stress σ_{ss} of HWRM could be estimated by its crack bridging stress $\hat{\sigma}_c$ and cracking stress level $\hat{\sigma}_{\mathrm{fc}}$ Based on the theoretical framework of fracture mechanics and micromechanics, both $\hat{\sigma}_c$ and $\hat{\sigma}_{\mathrm{fc}}$ are expressed as functions of crack size, with the following Eqs:

$$\frac{\hat{\sigma}_{\mathrm{c}}}{g}=\sqrt{2\bar{c}}-\frac{\bar{c}}{2} \tag{9}$$

$$\frac{\hat{\sigma}_{\mathrm{fc}}}{g}=\left(\frac{2\sqrt{2}}{3}\sqrt{\bar{c}}-\frac{\bar{c}}{4}\right)+\frac{\sqrt{\pi}}{2\bar{c}} \tag{10}$$

$$g=\frac{2}{4+f^2}\left(1+\mathrm{e}^{\pi\cdot f/2}\right) \tag{11}$$

where, σ_{c} is the surface closure stress induced by the fiber bridging effect at the crack surface of HWRM, and $\sigma_{\mathrm{c}}=\hat{\sigma}_{\mathrm{c}}\sigma_0$; σ_{fc} is the stress level at which each crack initiates during the multi-crack propagation behavior, and $\sigma_{\mathrm{fc}}=\hat{\sigma}_{\mathrm{fc}}\sigma_0$; f is the snubbing coefficient [57], with a value range from 0 to 1; σ_0 is calculated according to Eqs.(12), where τ_{i} is the interfacial bonding strength between fibers and the matrix, F_{be} is the fiber shape characteristic coefficient, and for straight steel fibers, it is taken as 1 [58].

$$\sigma_0=\frac{V_{\mathrm{i,pe}}\tau_{\mathrm{i,pe}}}{2}\left(\frac{l_{\mathrm{i,pe}}}{d_{\mathrm{i,pe}}}\right)+\frac{V_{\mathrm{i,sf}}\tau_{\mathrm{i,sf}}}{2}\left(\frac{l_{\mathrm{i,sf}}}{d_{\mathrm{i,sf}}}\right)\times F_{be}+\frac{V_{\mathrm{i,pp}}\tau_{\mathrm{i,pp}}}{2}\left(\frac{l_{\mathrm{i,pp}}}{d_{\mathrm{i,pp}}}\right) \tag{12}$$

When the crack bridging stress is equal to the matrix cracking stress, the material enters a multi-crack cracking state. Therefore, the stable cracking stress σ_{ss} can be expressed by the following equations:

$$\sigma_{ss} = \xi_1 g\left(\sqrt{2\bar{c}_s} - \frac{\bar{c}_s}{2}\right)\sigma_0 \tag{13}$$

$$\bar{c}_s = \frac{\sqrt{c_s / c_i}\cdot E_f \cdot (1+\eta) d_f}{2\tau l_f} \tag{14}$$

$$\eta = \frac{V_f E_f}{(1-V_f) E_m} \tag{15}$$

$$c_i = \left(\frac{l_f E_c}{2K_{tip}}\right)^2 \times \frac{\pi}{16(1-\upsilon^2)^2} \tag{16}$$

$$K_{tip} = (E_c / E_m) K_m \tag{17}$$

where, ξ_1 is stress correction factor considering the influence of solid waste substitution rate and ternary fiber hybrid system; c_s represents the characteristic crack size when multi-crack occurs; E_f is the fiber elastic modulus; η is the stiffness ratio between fiber and matrix; d_f is the fiber diameter; l_f is the fiber length; V_f is the fiber volume fraction; E_m is the elastic modulus of the matrix; K_{tip} is the fracture toughness at the crack tip; K_m is the fracture toughness of the matrix [59]; υ is Poisson's ratio.

The elastic modulus of HWRM in this study is calculated according to Eq.(18).

$$E_c = E_m (1-V_f) + \eta_l \eta_\theta E_f V_f \tag{18}$$

$$\eta_l = 1 - l_c / 2l_f \tag{19}$$

$$l_c = \frac{\sigma_{i,fu} d_i}{4\tau_i} \tag{20}$$

where, η_l is the length coefficient, when the fiber length l_f is less than or equal to the critical fiber length, η_l is taken as 0.5. However, when the fiber length is greater than the critical fiber length, η_l is calculated according to Eqs.(19)-(20) [59]; $\sigma_{i,fu}$ is the tensile strength of the fiber; η_θ is the orientation coefficient of freely distributed short fibers.

According to the study by Li et al. [57], the ultimate stress of HWRM can be calculated according to Eq.(21). Meanwhile, the study by Lin et al. [60] pointed out that the ultimate strain of HWRM can be calculated according to Eq.(22).

$$\sigma_{cu} = \xi_1 g \sigma_0 \tag{21}$$

$$\varepsilon_{cu} = \xi_2 \frac{\delta_{cu}}{x_d} \tag{22}$$

where, ξ_1 is stress correction factor considering the influence of solid waste substitution rate and ternary fiber hybrid system; ξ_2 is strain correction factor considering the influence of solid waste substitution rate and ternary fiber hybrid system; δ_{cu} represents the ultimate crack opening displacement; x_d is the ultimate crack spacing. This study assumes that under the ultimate state, the crack propagation within the gauge length of the specimen is uniform, the crack spacing is equal.

Relevant studies have shown that PE fibers exhibited slip hardening behavior under stress, while a small amount of PP fibers (content less than 1%) have no obvious slip hardening characteristics [61], and steel fibers exhibited slip softening behavior. Neglecting the slip hardening behavior of PE fibers will fail to reflect the characteristic that the bridging stress gradually increases with the increase of slip during the slip process, which will underestimate the deformation and toughening capacity of HWRM and result

in a lower calculated value of δ_{cu}. According to relevant studies, during the stress process, steel fibers exhibit slip softening behavior [62], while PE fibers exhibit slip hardening behavior. After comprehensive consideration, the value of δ_{cu} is based on the research results of Lin et al. [60], and δ_{cu} is approximately calculated according to Eqs.(23) and (24).

$$\delta_{cu} = \frac{l_f (c-2)}{6c} \tag{23}$$

$$c = \frac{\gamma l_f}{2d_f} \tag{24}$$

where, c is the crack radius; γ is a dimensionless hardening parameter that can be determined from the results of single fiber pull-out tests [63].

According to the study by Wu et al. [64], the theoretical value of the ultimate crack spacing in the fully saturated cracking state of the material should be calculated according to Eqs.(25) to (27). However, test results showed that the cracking state of HWRM was unsaturated, and its actual crack spacing was larger than the theoretical value. However, the introduction of the Weibull distribution function can effectively address this issue. Therefore, the ultimate crack spacing of HWRM could be calculated by Eqs. (28) to (30).

$$x_d^{theory} = \frac{l_f - \sqrt{l_f^2 - 2\pi\psi l_f x}}{2} \tag{25}$$

$$\psi = \frac{4}{\pi g} \tag{26}$$

$$x = \frac{V_m \sigma_{mu} d_f}{4 V_f \tau_i} \tag{27}$$

$$x_d = \frac{x_d^{theory}}{1 - F(\bar{c}_{mc})} \tag{28}$$

$$F(\bar{c}_{mc}) = \exp\left[-\frac{1}{\lambda} \left(\frac{\bar{c}_0}{\bar{c}_{mc}} \right)^m \right] \tag{29}$$

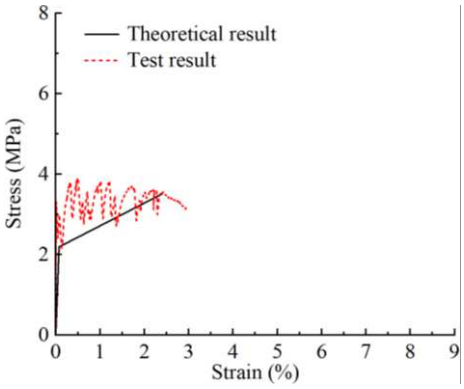
$$\bar{c}_0 = \left(\frac{\sqrt{\pi}}{2} \frac{K_m}{\sigma_{mu}} \right)^2 \tag{30}$$

where, σ_{mu} is the tensile strength of the matrix; m is the Weibull modulus; λ is a scale parameter derived from test results; $\bar{c}_{mc}$ represents the average crack length within the gauge length.

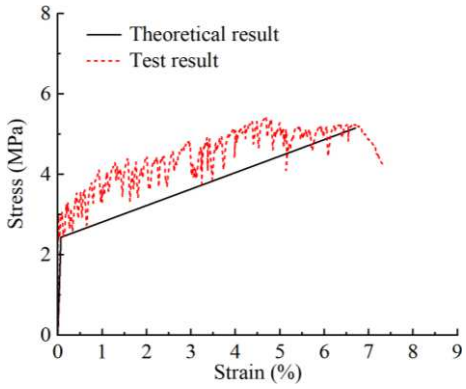
4.2 Model validation

Fig.11 shows the comparison between the calculated and test uniaxial tensile stress-strain curves of HWRM. By comparing the overall test curves and qualitative variations of key mechanical parameters, it was found that the established model in this study could well predict the tensile stress-strain relationship of HWRM. Error analysis indicated that the mean absolute percentage error (MAPE) of 3.48% for peak stress and 4.86% for peak strain. These results demonstrated strong consistency between numerical predictions and test data, verifying favorable accuracy of the proposed model. From the perspective of curve morphology, the model well reflected the essential characteristics of experimental curves. In the elastic stage, the calculated and test curves basically coincided with consistent slopes. In the plastic hardening stage, the model accurately followed the stress development trend of test curves

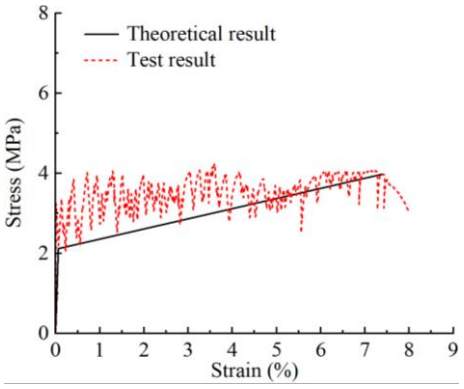
without obvious hysteresis or deviation. In the softening stage, the model properly captured the stress degradation trend of test curves. In summary, the numerical results were highly consistent with test data, which confirmed the high precision and reliability of the proposed constitutive model.



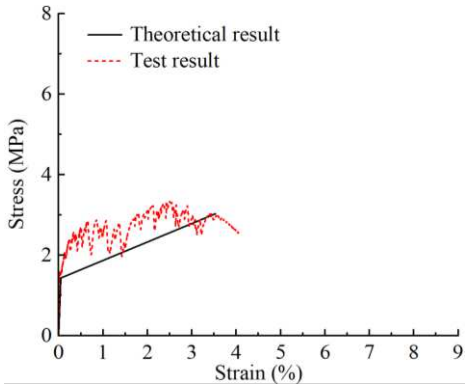
(a) $B_0W_0PE_2$



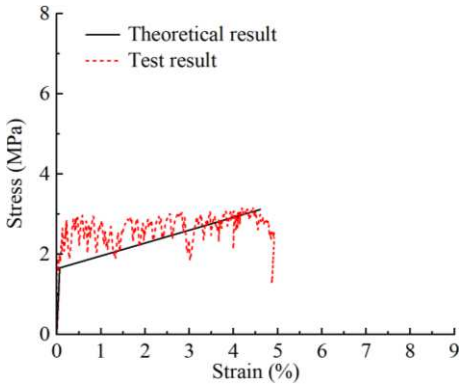
(b) $B_{10}W_0PE_2$



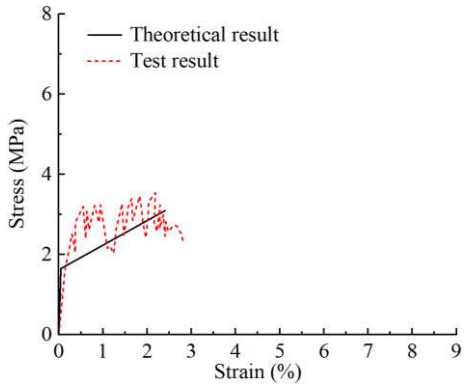
(c) $B_{30}W_0PE_2$



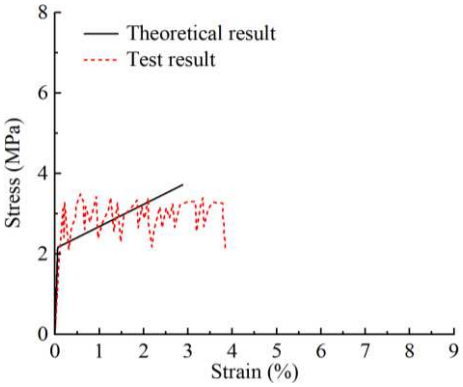
(d) $B_{50}W_0PE_2$



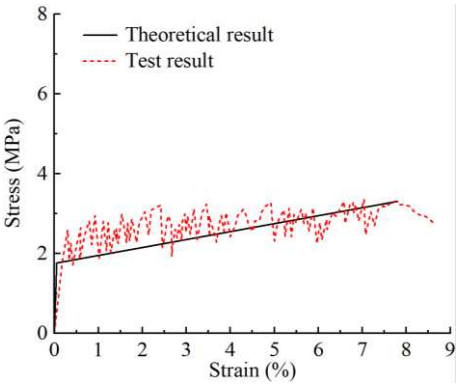
(e) $B_{70}W_0PE_2$



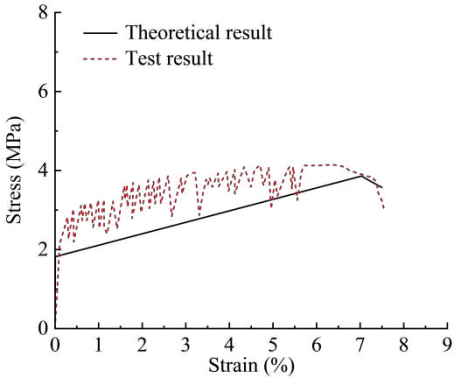
(f) $B_{45}W_{10}PE_2$



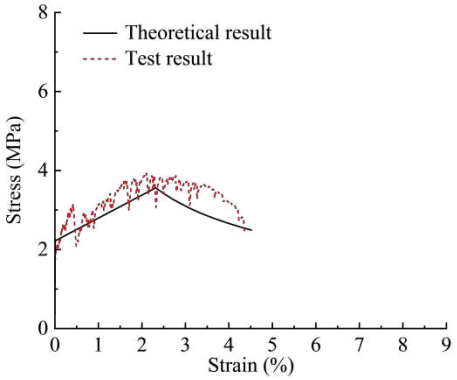
(g) $B_{40}W_{20}PE_2$



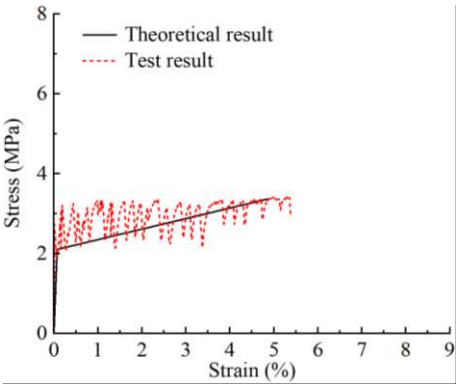
(h) $B_{35}W_{30}PE_2$



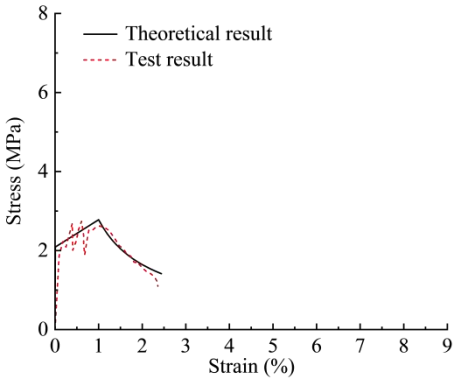
(i) $E_{1.5}S_{0.25}P_{0.25}$



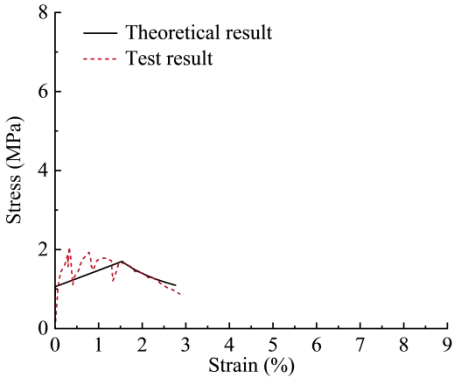
(j) $E_{1.5}S_{0.5}P_0$



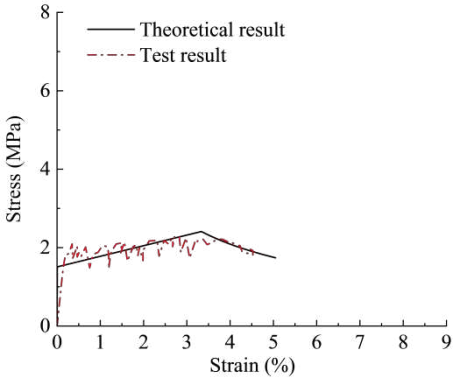
(k) $E_{1.5}S_0P_{0.5}$



(l) $E_1S_{0.75}P_{0.25}$



(m) $E_1S_{0.25}P_{0.75}$



(n) $E_1S_{0.5}P_{0.5}$

Fig.11. Comparison of theoretical and test results of stress-strain curves

5 Conclusion

This study used BFS and WGP as solid waste raw materials to prepare multi-scale hybrid fiber-reinforced high-content solid waste-based repair materials (HWRM). Macroscopic performance testing and microscopic mechanism analysis were systematically carried out, and the following conclusions were drawn：

(1) By using blast furnace slag and waste glass powder as solid waste raw materials, a high cement substitution rate of 65% can be achieved. The HWRM prepared has excellent fluidity, minimal negative impact of solid waste content on compressive strength, and good strength stability.

(2) The synergistic effect of multi-scale hybrid fibers significantly enhances the material's tensile deformation ability, with a maximum tensile strain of 7.8%, far superior to traditional ECC materials. Effectively achieved fine control of cracks, meeting the high ductility requirements of concrete structure repair.

(3) The microscopic results indicate that the rational combination of BFS and WGP can optimize the morphology of hydration products and the compactness of the matrix. PE fibers significantly enhance material ductility through bridging, sliding, and debonding effects. Excessive solid waste content can lead to loose hydration structure and performance degradation. Although mixed fibers enhance compressive strength, steel fibers are prone to defects when pulled out, which is not conducive to tensile deformation.

(4) The established tensile stress-strain theoretical model has a prediction accuracy of over 90% and can effectively characterize the mechanical evolution of materials. Provided theoretical basis for the design optimization of high solid waste green remediation materials and the promotion of practical remediation projects.

(5) In this study, equivalent interfacial bond parameters were derived from uniaxial tensile tests, while interfacial properties were not directly measured by single-fiber pullout tests and the influences of environmental actions on the long-term performance of HWRM were not examined. Further research will carry out single-fiber pullout tests to acquire interfacial indices and investigate the durability evolution of HWRM under environmental actions.

Acknowledgments

This study was funded by National Natural Science Foundation of China (52508545). The financial supports are greatly appreciated by the authors.

References

[1] Tu, H.X.; Xu, L.H.; Huang, L., et al. Performance degradation and strengthening of aged reinforced concrete beams subject to fatigue load: A state-of-the-art review. Compos. Struct. 387, 120322 (2026). https://doi.org/10.1016/j.compstruct.2026.120322

[2] Li, X.Y.; Xu, F.; Chen, B.G., et al. Investigation on the chloride ion erosion mechanism of cement mortar in coastal areas: From experiments to molecular dynamics simulation. Constr. Build. Mater. 350, 128810 (2022). https://doi.org/10.1016/j.conbuildmat.2022.128810

[3] Pandey, A.; Kumar, B. Investigation on the effects of acidic environment and accelerated carbonation on concrete admixed with rice straw ash and microsilica. J. Build. Eng. 29, 101125 (2020). https://doi.org/10.1016/j.jobe.2019.101125

[4] Xu, K.C.; Li, P.Q.; Huang, L.J., et al. Fatigue performance analysis and service life prediction of concrete exposed to simulated acid rain. Constr. Build. Mater. 521, 146139 (2026). https://doi.org/10.1016/j.conbuildmat.2026.146139
[5] Yu, P.; Wu, C.Z.; Yao, J.X., et al. Interfacial bond mechanical properties between normal concrete and UHPC/ECC under impact load. Constr. Build. Mater. 522, 146216 (2026). https://doi.org/10.1016/j.conbuildmat.2026.146139
[6] Felekoglu, B.; Tosun-K. Felekoglu, et al. Influence of matrix flowability, fiber mixing procedure, and curing conditions on the mechanical performance of HTPP-ECC. Compos. Part B-Eng. 60, 359-370 (2014). https://doi.org/10.1016/j.compositesb.2013.12.076
[7] Xu, L.Y.; Yu, J.; Huang, B.T., et al. Green and low-carbon matrices for Engineered/Strain-Hardening Cementitious Composites (ECC/SHCC): Toward sustainable and resilient infrastructure. J. Cleaner Prod. 496, 144968 (2025). https://doi.org/10.1016/j.jclepro.2025.144968
[8] Qi, J.A.; Wu, Z.M.; Ma, J.Z.G., et al. Pullout behavior of straight and hooked-end steel fibers in UHPC matrix with various embedded angles. Constr. Build. Mater. 191, 764-774 (2018). https://doi.org/10.1016/j.conbuildmat.2018.10.067
[9] Dong, S.F.; Gu, J.F.; Ouyang, X.Y., et al. Enhancing mechanical properties, durability and multifunctionality of concrete structures via using ultra-high performance concrete layer: A review. Compos. Part B-Eng. 297, 112329 (2025). https://doi.org/10.1016/j.compositesb.2025.112329
[10] Seo, J.; Kim, G.M.; Park, J., et al. Carbonation curing of ultra-high-performance concrete produced with Portland cement of varying belite content. Case Stud. Constr. Mat. 24, e05875 (2026). https://doi.org/10.1016/j.cscm.2026.e05875
[11] Ibrahim, M.S.; Solomon, Y.; Gebreyouhannes, E. Combined torsion and flexural behavior of FRP strengthened members: Model formulation and experiments. Eng. Struct. 357, 122516 (2026). https://doi.org/10.1016/j.engstruct.2026.122516
[12] Hu, T.Y.; Zhang, H.; Qiu, J.L., et al. Intelligent recognition of failure modes in fiber reinforced polymer strengthened reinforced concrete beams: Deep generative modeling and explainable machine learning. Eng. Appl. Artif. Intell. 172, 114340 (2026). https://doi.org/10.1016/j.engappai.2026.114340
[13] Kadhim, M.A.; Jawdhari, A.; Nadir, W., et al. Behaviour of RC beams strengthened in flexure with hybrid CFRP-reinforced UHPC overlays. Eng. Struct. 262, 114356 (2022). https://doi.org/10.1016/j.engstruct.2022.114356
[14] Zheng, X.C.; Sun, Q.; Liu, F., et al. Effects of industrial solid wastes on the rheological behavior and electrical resistivity-acoustic emission responses of cement-based grouted bodies under loading. J. Environ. Manage. 402, 128994 (2026). https://doi.org/10.1016/j.jenvman.2026.128994
[15] Zhu, J.Y.; Li, F.T.; Li, X.G., et al. Valorization of aluminum-silica-based industrial solid waste to high quality ceramic proppants: waste sources and design strategies. J. Cleaner Prod. 546, 147800 (2026). https://doi.org/10.1016/j.jclepro.2026.147800
[16] Liu, C.; Yan, C.W.; Zhang, Y.S., et al. Preparation of early strength concrete using all solid waste-based cement: Strength formation mechanism and carbon footprint evaluation. Constr. Build. Mater. 506, 145071 (2026). https://doi.org/10.1016/j.conbuildmat.2025.145071
[17] Chen, Y.Q.; Tong, X.Y.; Kang, X. Particle-chain structure induced by GO/MXenes enhances high iron ore tailings content-based alkali activated geopolymer unburned bricks. J. Build. Eng. 127, 116411 (2026). https://doi.org/10.1016/j.jobe.2026.116411

[18] Jin, S.H.; Ji, Y.C.; Wang, Z.H., et al. Modification mechanism and pile performance evaluation of coal gangue concrete with TRI-FA-Slag. J. Build. Eng. 123, 115792 (2026). https://doi.org/10.1016/j.jobe.2026.115792
[19] Chen, Y.Q.; Gan, Y.X.; Fu, X.S., et al. Towards a sustainable thermodynamic optimization solution for preparing unburned low-carbon bricks from low-activity tailings. J. Build. Eng. 98, 111206 (2024). https://doi.org/10.1016/j.jobe.2024.111206
[20] Jani, Y.; Hogland, W. Waste glass in the production of cement and concrete – A review. J. Environ. Chem. Eng. 2, 1767-1775 (2014). https://doi.org/10.1016/j.jece.2014.03.016
[21] Hamada, H.M.; Abed, F.; Katman, H.Y.B., et al. Effect of silica fume on the properties of sustainable cement concrete. J. Mater. Res. Technol. 24, 8887-8908 (2023). https://doi.org/10.1016/j.jmrt.2023.05.147
[22] Lu, H.B.; Tan, K.; Li, Y., et al. Synergistic reinforcement of foamed concrete using industrial waste stone powder and graphene oxide: Multi-scale characterization and field validation. Case Stud. Constr. Mat. 24, e06116 (2026). https://doi.org/10.1016/j.cscm.2026.e06116
[23] Song, X.T.; Li, B.C.; Fu, J., et al. Multi-objective optimization of mix design for geopolymer foam concrete with industrial solid wastes based on machine learning. J. Build. Eng. 123, 115878 (2026). https://doi.org/10.1016/j.jobe.2026.115878
[24] Du, Z.W.; Sheng, S.Q.; Guo, J.X. Effect of composite activators on mechanical properties, hydration activity and microstructure of red mud-based geopolymer. J. Mater. Res. Technol. 24, 8077-8085 (2023). https://doi.org/10.1016/j.jmrt.2023.05.049
[25] Luo, Y.P.; Jin, H.S.; Wang, D.F., et al. Fly ash-metakaolin-slag ternary cement replacement: Synergistic inhibition mechanism on concrete efflorescence and mechanical performance retention. J. Build. Eng. 124, 115984 (2026). https://doi.org/10.1016/j.jobe.2026.115984
[26] Li, J.X.; Fan, Z.X.; Tian, L., et al. Synergistic utilization of industrial solid wastes: Developing pervious concrete via an alkali-activated binder based on OPC, activated gold tailings, GGBS and coal gangue aggregate. Constr. Build. Mater. 506, 144967 (2026). https://doi.org/10.1016/j.conbuildmat.2025.144967
[27] GB/T 2419. Test method for fluidity of cement mortar. Standards Press of China, Beijing (2005).
[28] GB/T 17671. Test method of cement mortar strength(ISO method). Standards Press of China, Beijing (2021).
[29] Japan Society of Civil Engineers. Recommendations for design and construction of high performance fiber reinforced cement composites with multiple fine cracks (HPFRCC). Concrete Engineering Series No. 82, Japan Society of Civil Engineers, Tokyo (2008).
[30] Gong, Y.A.; Shao, C.Z.; Liu, R.T., et al. Recycling of waste glass powder: Effects on microstructure, mechanical properties and sustainability of seashell powder calcined sludge cement. J. Build. Eng. 96, 110665 (2024). https://doi.org/10.1016/j.jobe.2024.110665
[31] Xu, Y.C.; Xing, G.H.; Zhao, J.H., et al. The effect of polypropylene fiber with different length and dosage on the performance of alkali-activated slag mortar. Constr. Build. Mater. 307, 124978 (2021). https://doi.org/10.1016/j.conbuildmat.2021.124978
[32] Hu, X.Y.; Zheng, N.X.; Wang, X.W. Hybrid Fiber-Engineered Cementitious Composites (HFECCs) for Pavements: Performance and Application Insights. Int. J. Pavement Res. Technol. 19, 2312-2326 (2025). https://doi.org/10.1007/s42947-025-00580-x

[33] Meng, Z.X.; Li, L.; Farooqi, M.U., et al. Fiber factor for fresh and hardened properties of polyethylene fiber-reinforced geopolymer mortar. J. Build. Eng. 53, 104556 (2022). https://doi.org/10.1016/j.jobe.2022.104556
[34] Zhou, Y.W.; Xi, B.; Yu, K.Q., et al. Mechanical properties of hybrid ultra-high performance engineered cementitious composites incorporating steel and polyethylene fibers. Materials 11, 1448 (2018). https://doi.org/10.3390/ma11081448
[35] Li, S.C.; Sha, F.; Liu, R.T., et al. Properties of Cement-Based Grouts with High Amounts of Ground Granulated Blast-Furnace Slag and Fly Ash. J. Mater. Civ. Eng. 29, 04017219 (2017). https://doi.org/10.1061/(ASCE)MT.1943-5533.0002083
[36] Li, Z.J.; Zhan, J.Y.Y.; Wang, Y.J., et al. Low-carbon UHPC with glass powder and shell powder: Deformation, compressive strength, microstructure and ecological evaluation. J. Build. Eng. 94, 109833 (2024). https://doi.org/10.1016/j.jobe.2024.109833
[37] Liao, Q.; Yu, J.T.; Dong, F.Y., et al. Tension-shear characteristics, cost and environmental impact of polyethylene fiber reinforced engineered cementitious composites: The role of fiber content. Constr. Build. Mater. 428, 136312 (2024). https://doi.org/10.1016/j.conbuildmat.2024.136312
[38] Wu, Y.; Li, J.; Wu, K. Mechanical properties of hybrid fiber-reinforced concrete at low fiber volume fraction. Cem. Concr. Res. 33, 27-30 (2003). https://doi.org/10.1016/S0008-8846(02)00913-4
[39] Wan, Y.; Li, L.; Zou, J.X., et al. Effect of Shrinkage Reducing Agent and Steel Fiber on the Fluidity and Cracking Performance of Ultra-High Performance Concrete. Fluid Dyn. Mater. Process. 20, 1941-1956 (2024). https://doi.org/10.32604/fdmp.2024.053910
[40] Cao, M.L.; Xu, L.; Zhang, C. Review on micromechanical design, performance and development tendency of engineered cementitious composites. J. Chin. Ceram. Soc. 43, 632-642 (2015). https://doi.org/10.14062/j.issn.0454-5648.2015.05.12
[41] Xu, Y.W.; Wan, C.J.; Liang, X.H., et al. The reinforcement effects of PVA, PE, and steel fibers on AAS material. Case Stud. Constr. Mat. 17, e01386 (2022). https://doi.org/10.1016/j.cscm.2022.e01386
[42] Huo, Y.L.; Liu, T.A.; Lu, D., et al. Dynamic tensile properties of steel fiber reinforced polyethylene fiber-engineered/strain-hardening cementitious composites (PE-ECC/SHCC) at high strain rate. Cem. Concr. Compos. 143, 105234 (2023). https://doi.org/10.1016/j.cemconcomp.2023.105234
[43] He, H.J.; Gao, Y.F.; Yu, J., et al. Municipal solid waste incineration fly ash as activator for ground granulated blast-furnace slag: Hydration behavior and stabilization/solidification effectiveness. Case Stud. Constr. Mat. 23, e05177 (2025). https://doi.org/10.1016/j.cscm.2025.e05177
[44] Lu, J.X.; Duan, Z.H.; Poon, C.S. Combined use of waste glass powder and cullet in architectural mortar. Cem. Concr. Compos. 82, 34-44 (2017). https://doi.org/10.1016/j.cemconcomp.2017.05.011
[45] Yan, G.; Zhao, Y.; Wang, D.Z., et al. Mechanical enhancement of hybrid steel fiber-reinforced superabsorbent polymer concrete: Experimental and multiscale simulation analysis. J. Build. Eng. 117, 114762 (2026). https://doi.org/10.1016/j.jobe.2025.114762
[46] Ranjbar, N.; Zhang, M.Z. Fiber-reinforced geopolymer composites: A review. Cem. Concr. Compos. 107, 103498 (2020). https://doi.org/10.1016/j.cemconcomp.2019.103498
[47] Ying, X.J.; Zhao, J.J.; Ye, M., et al. Rice straw biochar–enhanced carbonation sequestration in recycled concrete: Influence of pyrolysis temperature and carbonation pressure. Case Stud. Constr. Mat. 24, e05846 (2026). https://doi.org/10.1016/j.cscm.2026.e05846

[48] Huang, H.Y.; Tan, H.B.; Wang, J., et al. Activation mechanism and performance of full solid-waste cementitious materials using modified concrete waste slurry as an activator. Case Stud. Constr. Mat. 24, e05951 (2026). https://doi.org/10.1016/j.cscm.2026.e05951

[49] Zhang, L.; Jia, Y.; Shu, H., et al. The effect of basicity of modified ground granulated blast furnace slag on its denitration performance. J. Cleaner Prod. 305, 126800 (2021). https://doi.org/10.1016/j.jclepro.2021.126800

[50] Dueramae, S.; Sanboonsiri, S.; Suntadyon, T., et al. Properties of lightweight alkali activated controlled Low-Strength material using calcium carbide residue – Fly ash mixture and containing EPS beads. Constr. Build. Mater. 297, 123769 (2021). https://doi.org/10.1016/j.conbuildmat.2021.123769

[51] Wang, D.; Fang, Y.F.; Zhang, Y.Y., et al. Changes in mineral composition, growth of calcite crystal, and promotion of physico-chemical properties induced by carbonation of β-C_2S. J. CO_2 Util. 34, 149-162 (2019). https://doi.org/10.1016/j.jcou.2019.06.005

[52] Lee, S.W.; Kim, Y.J.; Lee, Y.H., et al. Behavior and characteristics of amorphous calcium carbonate and calcite using $CaCO_3$ film synthesis. Mater. Design 112, 367-373 (2016). https://doi.org/10.1016/j.matdes.2016.09.099

[53] Oliveira, A.M.; Oliveira, A.P.; Vieira, J.D., et al. Study of the development of hydration of ternary cement pastes using X-ray computed microtomography, XRD-Rietveld method, TG/DTG, DSC, calorimetry and FTIR techniques. J. Build. Eng. 64, 105616 (2023). https://doi.org/10.1016/j.jobe.2022.105616

[54] Scrivener, K.; Snellings, R.; Lothenbach, B. A Practical Guide to Microstructural Analysis of Cementitious Materials. CRC Press Taylor & Francis Group, New York(NY) (2016).

[55] Zhang, C.; Xia, C.F.; Yuan, Z., et al. Tensile constitutive relationship of hybrid fiber reinforced strain-hardening cementitious composites. Acta Mater. Compos. Sin. 37, 1754-1762 (2020). https://doi.org/10.13801/j.cnki.fhclxb.20191114.001

[56] Ou, Y.C.; Tsai, M.S.; Liu, K.Y., et al. Compressive behavior of steel-fiber-reinforced concrete with a high reinforcing index. J. Mater. Civ. Eng. 24, 207-215 (2011). https://doi.org/10.1061/(ASCE)MT.1943-5533.0000372

[57] Li, V.C.; Leung, C.K.Y. Steady-state and multiple cracking of short random fiber composites. J. Eng. Mech. 118, 2246-2264 (1992). https://doi.org/10.1061/(ASCE)0733-9399(1992)118:11(2246)

[58] Zhang, C.; Han, S.C.; Yuan, H. Flexural performance of reinforced self-consolidating concrete beams containing hybrid fibers. Constr. Build. Mater. 174, 11-23 (2018). https://doi.org/10.1016/j.conbuildmat.2018.04.075

[59] Ahmed, S.F.; Maalej, M.; Paramasivam, P. Analytical model for tensile strain hardening and multiple cracking behavior of hybrid fiber engineered cementitious composites. J. Mater. Civ. Eng. 19, 527-539 (2007). https://doi.org/10.1061/(ASCE)0899-1561(2007)19:7(527)

[60] Lin, Z.; Li, V.C. Crack bridging in fiber reinforced cementitious composites with slip-hardening interfaces. J. Mech. Phys. Solids 45, 763-787 (1997). https://doi.org/10.1016/S0022-5096(96)00095-6

[61] Ahmed, A.H.; Hübner, J.; Junger, D., et al. Engineering low clinker Strain-Hardening cementitious composites (SHCC) using polyethylene and cost-effective polypropylene fibers: An experimental scale-linking analysis. Mater. Design 254, 114051 (2025). https://doi.org/10.1016/j.matdes.2025.114051

[62] Li, J.Y.; Deng, Z.C. Tensile behavior of ultra-high performance concrete reinforced with different hybrid fibers. Struct. Concr. 24, 1415–1435 (2023). https://doi.org/10.1002/suco.202200353
[63] Wang, Y.J.; Li, V.C.; Backer, S. Modelling of fibre pull-out from a cement matrix. Int. J. Cem. Compos. Lightweight Concr. 10, 143-149 (1988). https://doi.org/10.1016/0262-5075(88)90002-4
[64] Wu, H.C.; Li, V.C. Snubbing and bundling effects on multiple crack spacing of discontinuous random fiber-reinforced brittle matrix composites. J. Am. Ceram. Soc. 75, 3487-3489 (1992). https://doi.org/10.1111/j.1151-2916.1992.tb04457.x

Statements and Declarations

Funding

This study was funded by National Natural Science Foundation of China (52508545).

Competing Interests

The authors have no relevant financial or non-financial interests to disclose.

Author Contributions

All authors contributed to the study conception and design. *Jianjun Zhao*: Formal analysis, Supervision, Writing-original draft, Writing-review & editing, Funding acquisition, Methodology. *Xunxun Jiang*: Writing - original draft, Writing- Review & Editing, Formal analysis, Methodology. *Hao Chen*: Formal analysis, Methodology, Writing- Review & Editing. *Yisen Zhao*: Methodology, Writing-original draft. *Junhui Qiao*: Formal analysis, Methodology. *Shuang Li*: Methodology, Writing-original draft, Writing-review&editing.

Data Availability

All data used during the study appear in the submitted article.